Technical Memo

ECMWF
European Centre for Medium-Range
Weather Forecasts

874

Experimenting with a clear air turbulence (CAT) index from the IFS

P. Bechtold[1], M. Bramberger[2], A. Dörnbrack[2], L. Isaksen[1], M. Leutbecher[1]

[1] Research Department, ECMWF,
[2] DLR, Oberpfaffenhofen, Germany

January 2021

Abstract

A calibrated diagnostic of clear air turbulence (CAT) in the free troposphere and stratosphere has been developed in the ECMWF Integrated Forecast System (IFS) using Cy47r1 and the new moist physics for Cy48r1. The diagnostic largely follows the method proposed by Sharman and Pearson (2017), whereby predictors for turbulence are projected onto the climatological distribution of the EDR ($m^{2/3}s^{-1}$) whis is defined as the cube root of the turbulent eddy dissipation rate.

We computed several indices from daily 0-24 h high resolution (9 km) forecasts of the IFS and compared during January to March 2019 their distribution to civil aircraft data from the NOAA Meteorological Assimilation Data Ingest System (MADIS) in the height range of 5-12 km using model level data. In addition, the IFS ensemble was run at 18 km resolution during the first 14 days of January 2019 allowing to evaluate the ensemble mean and probabilistic skill of turbulence forecasts. It is found that a CAT based on a modified Ellrod1 index and/or the total dissipation rate that is derived from the subgrid physical momentum tendencies of the IFS, provide useful guidance for severe turbulence. Point correlations with observations from the high-resolution system of 0.34 and 0.31 (0.35 combined) were obtained for the two CAT (EDR) products and a mean absolute error of 0.055 $m^{2/3}s^{-1}$. Encouraging results come from the ensemble forecasts with ensemble mean correlations above 0.4 for January and a continuous rank probability score of below 0.03 $m^{2/3}s^{-1}$. Overall, the EDR point correlations are in between the point correlations of 0.53 for 10 m wind speed and 0.2-0.4 for daily tropical rainfall over land as obtained from 24h forecasts.

Given archiving and computing constraints and the needs of a direct validation of the IFS turbulence scheme, we decided to only put the CAT based on the total dissipation rate into operations. This product should also be of interest in a future ERA6 climate reanalysis. The information provided in this document is also intended to enable user specific postprocessing including the computation of CAT based on Ellrod1, as well as advanced postprocessing using non-linear regression and/or machine learning.

1   Motivation

Forecasting severe turbulence in the free troposphere and stratosphere is challenging. The turbulence is generated by processes such as shear instabilities (Kelvin Helmholtz instabilities), upper-level frontogenesis, large amplitude mountain waves and breaking of convectively generated gravity waves (Ellrod and Knapp, 1992; Lane et al., 2004; Williams and Joshi, 2013). In particular, turbulent eddies and waves with length scales of a hundred meters to several kilometers pose an important hazard to civil aviation, hence there is a great demand in aviation forecasting for reliable turbulence estimates (Sharman et al., 2014). The EDR which is the cube root of the dissipation rate of turbulent kinetic energy has become the International Civil Aviation Organization (ICAO) standard for aircraft reporting. A recent survey among the ECMWF forecast user community collected by T. Hewson and colleagues has revealed that a CAT parameter has a high priority on the user wish list, just below convection. Furthermore, for research purposes, in particular the development of turbulence parametrizations in the free troposphere and stratosphere, it is important for us to have an observable turbulence diagnostic that goes beyond the already existing parameters such as the diffusion coefficients for heat and momentum and the local Richardson number.

2   Method

Following the method presented in Sharman and Pearson (2017) we have computed the distributions of turbulent predictors using Cy47r1 together with the new moist physics branch. A log-normal distri-

bution has then been fitted to the distribution of each individual parameter and finally each parameter is converted into units of EDR by projecting its distribution onto a climatological distribution of EDR. However, in contrast to the ensemble global graphical turbulence guidance products on a 0.25°-0.5 ° grid with 1 km vertical bins developed by Sharman and Pearson (2017) and Kim et al. (2018), the present study is restricted to just a few parameters in order to experiment with and construct the CAT product. Instead, we use high-resolution and ensemble data on model levels (with a typical grid-spacing of 300 m in the upper-troposphere and lower stratosphere) and on a reduced output grid (0.1 ° for establishing the pdfs and 0.3 ° for verification) given the huge data volume. As reported by Kim et al. (2018) it is planned to have by 2030 a turbulence guidance product for the ICAO global navigation plan at 0.1 ° horizontal and 300 feet vertical resolution.

The selected turbulence parameters are summarized below, while their detailed formulations are provided in the Appendix.

- Ellrod1: The positive definite Ellrod1 index has beed developed by Ellrod and Knapp (1992). It is the product of the vertical wind shear with the total deformation and is distinguished from the Ellrod2 index that also contains a divergent term. The terms involving horizontal gradients are still small at 10 km resolution compared to the vertical gradients. However, using their product has been shown to improve the correlationis compared to using the vertical shear term only (Ellrod and Knapp, 1992). The Ellrod1 index is of valued guidance in aviation forecasting and was also shown to be the best performing index in Sharman and Pearson (2017).

- F3D: three-dimensional frontogenetic function (Holton, 2004) (pp. 269-276), but where we have neglected the terms including the horizontal derivatives of the vertcial velocity and terms relating to the derivatives of the diabatic heating.

- MWT3: mountain wave index, the product of F3D with the wind speed above the boundary-layer times the orographic elevation. The orographic elevation is capped to 2800 m and the index is only computed if the standard deviation of subgrid orography exceeds 10 m.

- GWD: While the above parameters account for resolved flow features, we propose to also include a subgrid contribution from breaking convectively generated gravity waves (GWD). A simple approach is to scale the dissipation rate from the non-orographic gravity wave scheme (having a globally uniform departure wave spectrum) with the normalised vertically integrated convective heating between 500 hPa and the cloud top. The cube root of the dissipation then readily gives units of EDR.

- *Ri*: The local Richardson number.

- DISS: The total dissipation rate of the IFS in units of EDR is derived from the model's physical tendencies for horizontal momentum. It includes contributions from the vertical diffusion scheme, the convective momentum transport and the convective gravity wave drag GWD. The largest contribution to the total dissipation is from the vertical diffusion scheme that includes dissipation due to turbulent mixing, orographic wave drag and orographic blocking (Louis, 1979; Beljaars et al., 2004). We have also tried to include a dissipation contribution from the model dynamics, but this proved so far detrimental to the correlations.

The horizontal gradients for *u* and *v* wind components are derived from vorticity and divergence. Additional inverse spectral transforms are necessary in the IFS to obtain the vorticity, divergence and the horizontal temperature gradient in grid point space. The additional spectral transforms increase the total forecast time by 4-5% under limited field output.
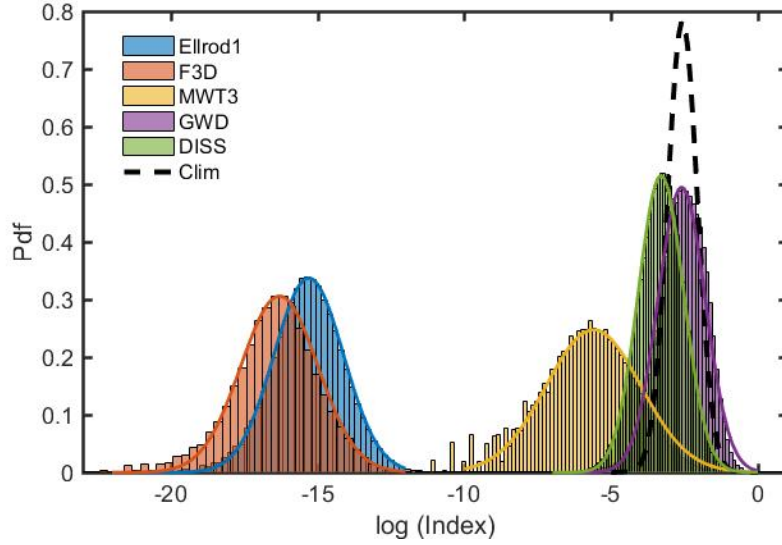
Figure 1: Pdf's of the logarithm of the Ellrod1, F3D, MWT3, GWD and DISS indices for the atmospheric layer between 600 and 150 hPa (4.5-15 km) as obtained from 6 months of TCo1279 (9 km) IFS simulations for 2019. The solid lines denote the fits by a log-normal distributiom. The climatological EDR distributions as used in (3) is denoted by the black curve.

Figure 1 shows the Pdfs of the logarithm of Ellrod1, F3D, MWT3, GWD and DISS as obtained from 24 h simulations with the IFS at resolution TCo1279 (9 km) during the first six months of 2019. The distributions are valid for the 4.5-15 km atmospheric layer. Generally, the selected indices in Figure 1 closely follow a log-normal law. The Ri number has not been included in Figure 1 as its distribution significantly deviates from a log-normal distribution. It will be used in its non-dimensional form, i.e. without EDR projection. Also included in Figure 1 are the log-normal fits (solid lines) for the parameter distributions following the distribution function

$$Y = \frac{1}{\sqrt{2\sigma^2\pi}} \exp\left(-\frac{(X-\mu)^2}{2\sigma^2}\right); \quad \mu = <\ln(x)> \tag{1}$$

where $X = \ln(x)$, with x the actual or physical value for each index. The parameters μ and σ^2 represent the mean and variance, respectively. Their values for each index are listed in the Appendix in Table 2.

Having computed the log-normal fits, each turbulence index is then projected onto the climatological distribution of EDR

$$\ln(y^*) = a + b\ln(x); \quad y^* = e^a x^b \tag{2}$$

where x stands for the original turbulence index and y^* for the transformed index in EDR. The transformation coeffcients a and b are given by

$$b = \frac{c2}{\sigma}; \quad a = c1 - b\mu \tag{3}$$

with the constants $c1 = -2.57$ and $c2 = 0.51$ representing the climatological mean and standard deviation of the EDR as proposed in Sharman and Pearson (2017).

We have also overlaid in Figure 1 the climatological distribution as used in the projections (3). The DISS and GWD parameters which naturally have units of EDR have distributions similar to the climatological

EDR, but with a significantly larger variance. Finally, note that the correlation of the index with the EDR observations will be mainly determined by the suitability of the index itself and is only weakly affected by the climatological EDR projection.

3   Observations

We have retrieved max EDR that is the peak EDR from the NOAA/MADIS public archive for airacraft data. The dataset and algorithm onboard civil aircraft to compute EDR is thoroughly described in Sharman et al. (2014) and Cornman et al. (1995). In summary, the aircraft response to turbulent eddies with wavelengths of 10 m to 1 km is felt as bumpiness. The aircraft is more sensitive to vertical gusts than to lateral gusts (Hoblit, 1988)(i.e. the steering is more sensitive in the vertical as aircraft built to be stable in the lateral axis). The EDR is proportional to the root-mean-square vertical acceleration experienced by an aircraft under specific flight conditions. The EDR algorithm either uses the measured vertical accelerations or the aircraft measured vertical winds (G. Meymaris, 2019 personal communication). For the latter a Fourier transform is performed on the 8 Hz sampled time series (with a cruise speed of 250 m s^{-1} this retains eddies of 30 m that can significantly affect the aircraft wings) and a von Kármán spectrum is fitted to the retrieved vertical velocity spectrum in the inertial turbulent subrange. When the algorithm detects a turbulent event a report is generated and downlinked at a 1 min ($\approx$15 km) interval, follow up reports are then also generated.

In order to compare the IFS with the observations, we have performed daily 24 h forecasts for January to March 2019 and used hourly model output on the full vertical model resolution of 137 levels but on a reduced horizontal grid of $0.3° \times 0.3°$ to make the data volume more managable. The comparison focuses on the height range 5-12 km, i.e. the cruising altitude, where the IFS vertical resolution is roughly 300 m. The projection of the forecast onto the observations is done by retaining all observations 15 minutes before and after the full hour and allowing a maximum height difference between observations and model data of 160 m.

We had to account for the fact that out of the more than 4 million observations onto which the IFS data has been projected, a large majority has zero value, while the model is producing a continuous field. We therefore included a EDR threshold of 0.005 m$^{2/3}$ s^{-1} for the observations, therefore being able to retain only 197000 observations for the statistics. The statistics are, however robust, even for a single month.

4   Definition of CAT

Given the above turbulence indices, we have experimented with different combinations to obtain a CAT product that best matches the observations in terms of correlations or mean absolute errror. It appeared that the best correlation with the observations is obtained from Ellrod1 and DISS. Only combinations with GWD slightly improve the correlations, while combinations with all other indices, including F3D, significantly degrade the correlations. Furthermore, a specific mountain wave index such as MWT3 appeared to be particularly difficult to verify and we have dropped the idea of retaining a specific mountain wave index for the IFS. The results of different CAT definitions based on Ellrod1, GWD and/or DISS
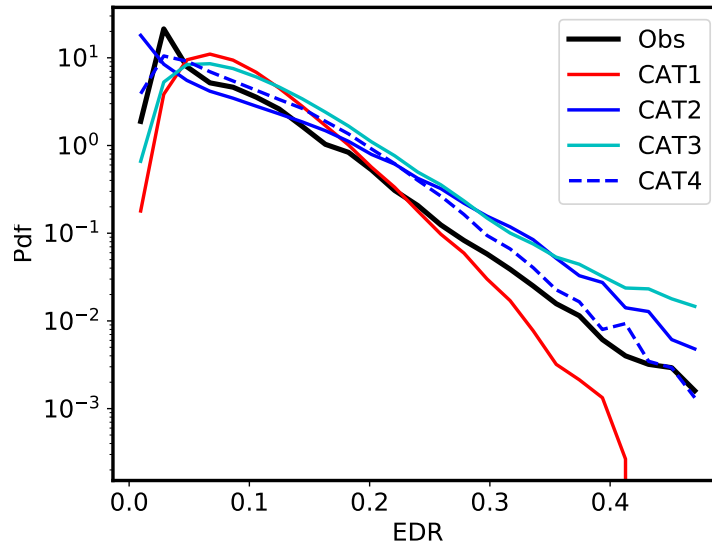
Figure 2: Pdf's of EDR as obtained from the NOAA/MADIS dataset for January, March, June 2019 for heights between 5 and 12 km and the corresponding PDf's for CAT1 (red) and CAT (blue) as obtained from IFS data projected onto the observation locations. Only observations with EDR > 0.005 $m^{2/3}$ s^{-1} have been retained.

will be discussed further and include

$$\text{CAT1} = 0.6\,\text{Ellrod1}^* + \text{GWD}^*$$
$$\text{CAT2} = 0.85\,\text{Ellrod1}^*\,\min(1, 0.5\,\text{Ri}^{-1}) + \text{GWD}^*$$
$$\text{CAT3} = 0.6\,\text{DISS}^*$$
$$\text{CAT4} = 0.5\,(CAT2 + CAT3)$$

(4)

where the superscript $*$ denotes the value of the respective index after projection onto the climatological EDR. Further leading scaling factors have been introduced in (4) to scale the mean of the distribution to that of the current MADIS dataset. This is necessary as the model produces stronger vertical wind shear and turbulence in winter compared to summer, while the climatological projection is valid for annual mean turbulence intensity. The non-dimensional Ri number with Ri$> 10^{-6}$ has been retained for the scaling of Ellrod1* in CAT2 in order to correct for a general overforecasting of small values of EDR ($<0.1\text{m}^{2/3}$ s^{-1}) for which the MADIS datasets suggests an exponential instead of log-normal law. Estimations of the observed maximum EDR using either CAT2 or CAT3 differ fundamentally as CAT1,2 are based on properties of the resolved flow, while CAT3 is based on the unresolved (parametrized) part of the flow.

The Pdfs of the observations and the corresponding projected IFS data for the different EDR estimates are displayed in Figure 2 including a total of 196000 observations with EDR values above 0.005 m$^{2/3}$ s^{-1}. Both CAT1 and CAT3 underestimate the relative occurence of light turbulence around < 0.1 m$^{2/3}$ and small turbulence values s^{-1} compared to the observations which is due to the log-normal projections, this is corrected for with CAT2. Overall, the distributions of CAT2 and CAT3 and in particular that of CAT4 which is their linear combination, broadly follow the observed distribution.
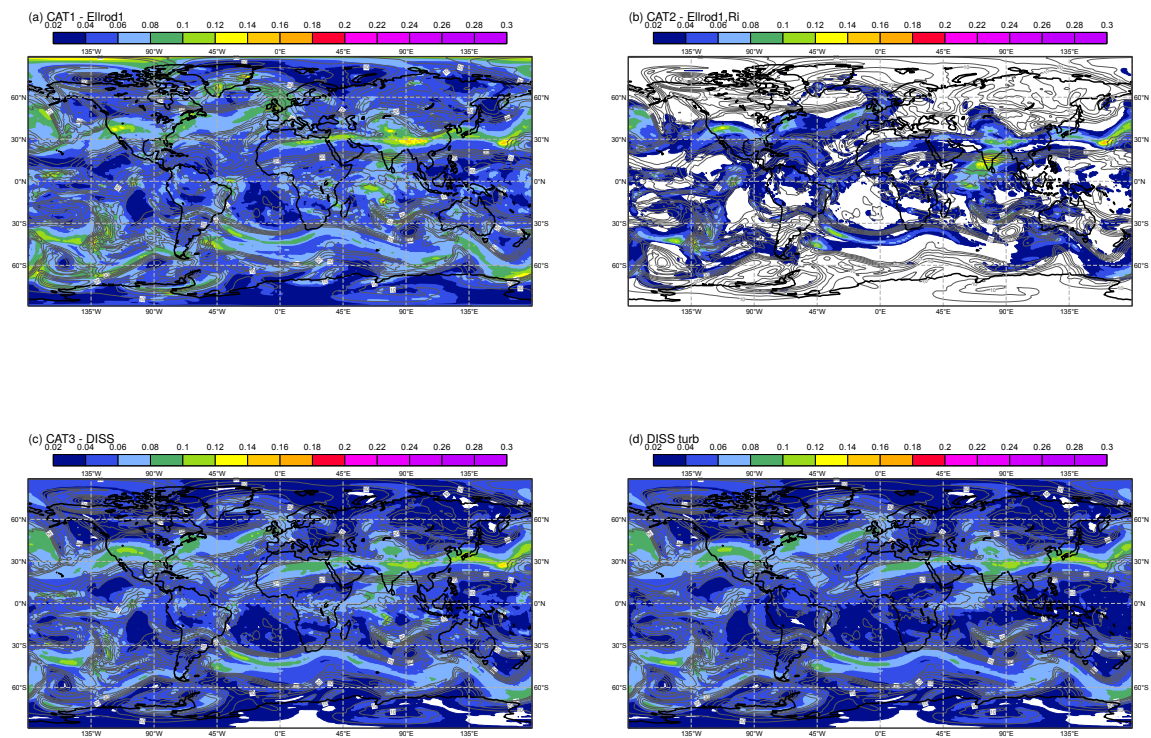
Figure 3: Global daily mean distributions of (a)-(c) CAT1-3 and (d) the turbulent dissipation only, for 2 March 2019 averaged over the 10-12 km layer. Shadings are in units of EDR, with the isotachs of 250 hPa wind speed are overlaid by black contours.

5 Global maps and case study

The purpose of the case study is to illustrate global maps of the different model derived EDR diagnostics and their individual contributions as defined in 4 and the Appendix. Mean values of CAT1, CAT2, CAT3 and the contribution of the turbulent dissipation to CAT3 are shown in Figure 3a-d, respectively. The mean values are computed over the 10-12 km altitude layer and over 24 h for a forecast valid on 2 March 2019 (0-24UTCh). To illustrate the role of wind shear the 250 hPa, isotachs have also been included in Figure 3.

While the absolute values of the different estimates depend on the respective scaling factors applied in (4), we notice in Figure 3 that the global distribution of EDR is very similar between the independent products CAT1,2 and CAT3. Maximum daily and layer mean values of between 0.1 and 0.18 are present near the flanks of the subtropical jets and in the storm tracks, but also over orography such as the Rocky mountains and the Himalayas. Compared to CAT1, CAT2 more strongly distinguishes turbulent from non turbulent regions. We also notice significant EDR in tropical regions, especially near the equator and in convective regions over land. The convective contribution to CAT2 stems from the convective gravity wave drag, while for CAT3 it also includes a contribution from convective momentum transport. Comparing Figure 3c that corresponds to the total dissipation rate with Figure 3d, where only the turbulent and orographic contribution to the total dissipation is included, we notice the dominance of the latter in the extra tropical regions and over mountainuous regions, while the contribution from convective processes is significant in tropical regions.

A comparison with all non-zero EDR reports between 5 and 12 km altitude for 2 March 2019 is presented in Figure 4. The different CAT are generally able to predict the turbulence regions over the southern Rockies, northern Florida and also the observed elevated turbulence over the central US, southern Greenland and the northeastern Atlantic. However, there are larger differences between the different CAT in predicting the high turbulence regions with observed EDR above 0.3 $m^{2/3}s^{-1}$, depending also on the scaling factors used in (4) and the sharpness of the distributions. While all CAT products tend to over-predict turbulence, CAT4 seems to perform best. There is however a likely low bias in the observations as aircraft try to avoid and/or rapidly quit regions with strong turbulence.

6 Discussion and evaluation

The forecast verification dataset includes 3 months of high-resolution data and 14 days during January from a 15 member ensemble. All data has been reduced to a $0.3 \times 0.3°$ output grid on model levels. The verification statistics for the different EDR products are listed in Table 1. The 3-months average correlation from the high-resolution forecasts with the observations ranges from 0.30 for CAT3 to 0.34 for CAT2 and 0.35 for the combined product CAT4, while the mean absolute error (MAE) ranges from 0.057 $m^{2/3}s^{-1}$ for CAT3 to 0.048 for CAT2 and 0.047 for CAT4. CAT1 is in all scores slightly worse than CAT2.

In Table 1 we also compare the high-resolution performance for the period 1-14 January to the performance of the ensemble. 19600 observations with EDR$> 0.005 m^{2/3}s^{-1}$ have been used for the verification including as metrics the correlation of the ensemble mean with the observations and the continuous ranked probability score CRPS. The CRPS evaluates the mean square difference of the cumulative distribution function (cdf) of the probabilistic forecast with the cdf of the observations (Heaviside function). The CRPS of the ensemble directly compares to the MAE of the high-resolution forecasts. We notice in Table 1 that the ensemble forecasts behave as expected in that the ensemble mean correlations are
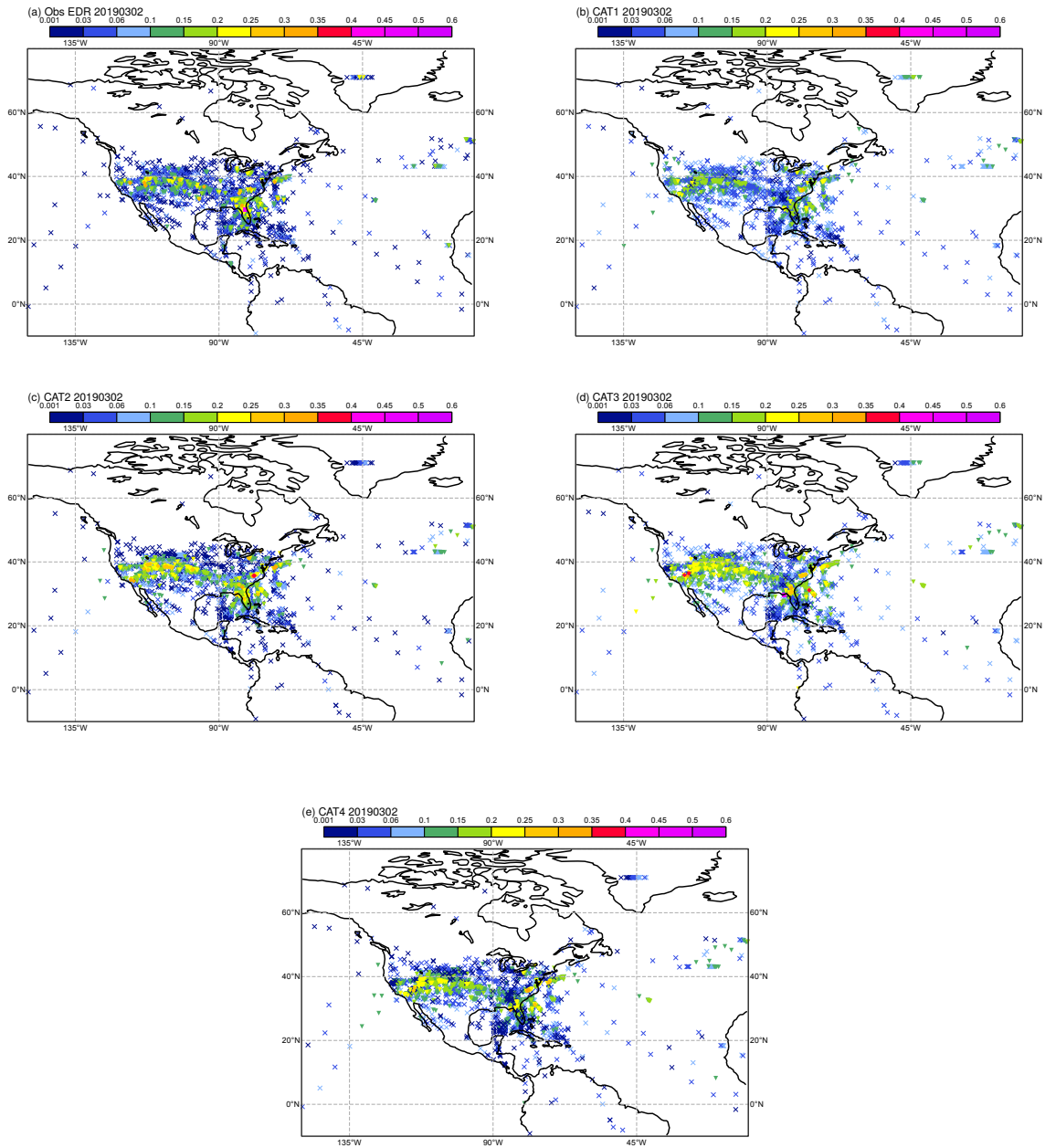
Figure 4: EDR for 2 March 2019 between 5 and 12 km as (a) observed and (b)-(e) from four different CAT products computed from a 0-24 h high-resolution forecast with the IFS. Colours (see legend) and symbols are used to denote the strength of the EDR, with different symbols for each 0.1 interval of EDR.

EDR parameter	Corr Hres Jan-Mar	MAE Hres Jan-Mar	Corr Hres 1-14 Jan	Corr Ens 1-14 Jan	MAE Hres 1-14 Jan	CRPS 1-14 Jan
CAT1	0.33	0.050				
CAT2	0.34	0.048	0.36	0.39	0.050	0.031
CAT3	0.30	0.057	0.32	0.37	0.054	0.034
CAT4	0.35	0.047	0.38	0.41	0.047	0.028

Table 1: Verification of different EDR parameters against observations for the high-resolution (Hres) forecasts for January-March 2019 and for the ensemble forecasts for the period 1-14 January 2019. Verification statistics are correlation (Corr), mean absolute error (MAE) and continuous ranked probability score (CRPS).

typically 0.03 higher than the respective high-resolution correlations attaining values of up to 0.41 for CAT4. The ensemble particularly improves the results for CAT3, increasing the correlation from 0.32 for the high-resolution to 0.37 in the ensemble mean. This is somehow expected as CAT3 is based on model tendencies which are particularly variable in time, while CAT1 and CAT2 are based on model state variables. Comparing the CRPS to the MAE we notice a significant error reduction from values around 0.05 $m^{2/3}s^{-1}$ for the MAE to values of 0.03 $m^{2/3}s^{-1}$ or below for the CRPS.

The improvements in forecast quality brought by the ensemble for a highly stochastic variable like max EDR are also illustrated by the two-dimensional density distributions in Figure 5 of ensemble mean forecast of CAT4 versus observations and (b) high-resolution forecasts versus observations. While there is large scatter in the high-resolution forecasts, the verification data for the ensemble mean is more concentrated around the main diagonal.
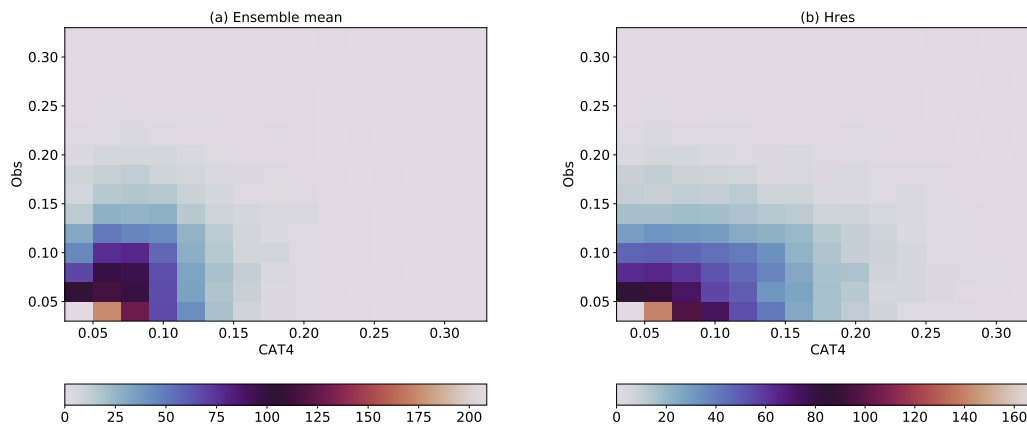

Figure 5: Normalized two-dimensional histogram of CAT4 versus observations for January 1-14 2019 as from (a) the ensemble mean and (b) the high-resolution forecasts

The subjective evaluation of CAT against aircraft data for many days reveals useful turbulence guidance for forecasters. Overall, the best results are obtained for the combined EDR estimate CAT4, while the results for the model derived dissipation rate CAT3 are slightly inferior but comparable. It is hoped however that when using a full 50-member ensemble a sufficiently reliable EDR estimate can be obtained based on CAT3 alone. The results reported here can be loosely compared to the correlations above 0.4

reported by Ellrod and Knapp (1992) using pilot reports (PIREP) and to the reliabilities of around 0.6, with overforecasting of turbulence, reported by Sharman and Pearson (2017) using an ensemble method but lower model resolution. Interestingly, the EDR correlations reported here are similar to the 0.2-0.4 point correlations obtained for another highly uncertain and stochastic quantity, namely 24h tropical rainfall forecasts over land (Thomas Haiden, personal communication).

7   Conclusions

We think there is now sufficient evidence that a simple EDR diagnostic derived from the IFS is a useful addition to the standard IFS output for both forecasters and for research in turbulence, particularly when used in the context of ensembles. We also think that such a turbulence diagnostic would be interesting for the next climate reanalysis ERA6.

Given archiving and computing constraints and the need for a direct validation of the IFS turbulence scheme, we propose to put the total dissipation rate as a meaningful predictor for Clear Air Turbulence into operations. The total dissipation rate is also a more useful CAT predictor in the planetary boundary-layer than the Ellrod1 index. All turbulent indices presented in this document are available in the code for Cy48r1 under optional switches. The information provided in this document should enable users to compute also online or offline a CAT product based on Ellrod1 and enable advanced postprocessing using non-linear regression and/or machine learning.

Acknowledgements

8   Appendix

8.1   Ellrod index

The Ellrod1 index (Ellrod and Knapp, 1992) is defined as the product of the vertical shear and the horizontal deformation of the horizontal wind field

$$\text{Ellrod1} = \left[\left(\frac{\partial u}{\partial z}\right)^2 + \left(\frac{\partial v}{\partial z}\right)^2\right]^{1/2} \left[\left(\frac{\partial v}{\partial x} + \frac{\partial u}{\partial y}\right)^2 + \left(\frac{\partial u}{\partial x} - \frac{\partial v}{\partial y}\right)^2\right]^{1/2} \tag{5}$$

The meridional velocity gradients are obtained in the IFS through

$$\frac{\partial u}{\partial y} = \frac{\partial v}{\partial x} - \zeta; \quad \frac{\partial v}{\partial y} = -\frac{\partial u}{\partial x} + \delta \tag{6}$$

where ζ and δ are the vorticity and divergence, respectively

All notations are standard, u and v denote the wind components in the zonal, x and meridional, y direction, respectively and z is height.

8.2 Three dimensional frontogenetic index

$$
\text{F3D} = \frac{1}{|\nabla\theta|}\left[\frac{\partial\theta}{\partial x}\left(-\frac{\partial u}{\partial x}\frac{\partial\theta}{\partial x}-\frac{\partial v}{\partial x}\frac{\partial\theta}{\partial y}-\frac{\partial w}{\partial x}\frac{\partial\theta}{\partial z}\right)+\frac{\partial\theta}{\partial y}\left(-\frac{\partial u}{\partial y}\frac{\partial\theta}{\partial x}-\frac{\partial v}{\partial y}\frac{\partial\theta}{\partial y}-\frac{\partial w}{\partial y}\frac{\partial\theta}{\partial z}\right)\\+\frac{\partial\theta}{\partial z}\left(-\frac{\partial u}{\partial z}\frac{\partial\theta}{\partial x}-\frac{\partial v}{\partial z}\frac{\partial\theta}{\partial y}-\frac{\partial w}{\partial z}\frac{\partial\theta}{\partial z}\right)\right]
\tag{7}
$$

where θ is the potential temperature and w the vertical velocity. We have set the horizontal gradients of the vertical velocity to zero and $\partial w/\partial z = -\delta$.

8.3 Mountain wave turbulence

The index for mountain wave turbulence uses a simple product of F3D, lower tropospheric wind speed and orographic elevation H

$$
\text{MWT3} = \text{F3D}\min(2750, H)\, V_{850}
\tag{8}
$$

where V_{850} is the maximum wind speed in the 500-1500 m layer above the surface. F3D is only computed for grid points where the standard deviation of the subgrid orography exceeds 10 m.

8.4 Dissipation from convectively generated gravity waves

We make the very simplified assumption of a prescribed globally uniform launch spectrum where the convection ony changes the amplitude of the wave spectrum. We then simply scale the already computed dissipation from the non-orographic gravity wave scheme (Orr et al., 2010) with the integrated convective heating between 500 hPa and the convective top. This assures that only heating from penetrative convection contributes to the generation of turbulence.

$$
\text{GWD} = \left[\left|\left(u\frac{\partial u}{\partial t}\big|_{\text{gwd}}+v\frac{\partial v}{\partial t}\big|_{\text{gwd}}\right)\right|\hat{T}_{\text{conv}}\right]^{1/3};\quad \hat{T}_{\text{conv}} = -\frac{c_{\text{p}}}{\hat{T}_0}\int_{p=500}^{top}\frac{\partial T}{\partial t}\big|_{\text{conv}}\frac{dp}{g}
\tag{9}
$$

where the subscript gwd denotes the tendencies (wave drag) from the non-orographic wave scheme and the subscript conv the temperature tendency from the convection parametrization, g is gravity and $c_{\{\text{p}}$ the specific heat at constant pressure. $\hat{T}$ is normalized by $\hat{T}_0 = 1$ W m^{-2}. Thus, GWD and EDR have the same dimensions.

8.5 The gradient Richardson number

The local Richardson number is defined as

$$
Ri = \frac{g}{T_v}\frac{\partial T_v/\partial z + g/c_{\text{p}}T_v/T}{(\partial u/\partial z)^2 + (\partial v/\partial z)^2}
\tag{10}
$$

where T_v is the virtual temperature.

8.6 Total dissipation rate

The total dissipation rate is estimated as the sum of the turbulent dissipation rate and contributions from convective momentum transport and convective gravity wave drag. The turbulent dissipation rate is by far the dominant term. It is derived from the vertical diffusion tendencies for momentum of the IFS which contain contributions due to turbulent mixing, orographic wave drag and orographic blocking.

$$\text{DISS} = \left| \left(u \frac{\partial u}{\partial t}|_{\text{diff}} + v \frac{\partial v}{\partial t}|_{\text{diff}} \right) \right|^{1/3} + \left| \left(u \frac{\partial u}{\partial t}|_{\text{conv}} + v \frac{\partial v}{\partial t}|_{\text{conv}} \right) \right|^{1/3} + \text{GWD} \tag{11}$$

where subscript diff denotes the tendencies for horizontal momentum from the vertical diffusion scheme and the subscript conv the tendencies due to convective momentum transport. DISS naturally has units of EDR, but is strictly only defined as the vertical integral of (11). In order to get positively definit values for each level, we chose to retain the absolute value of the kinetic energy tendency. Note that Shutts (2015) used a different formulation of the convective dissipation rate that is proportional to the product of the square of the updraught vertical velocity and the convective detrainment rate. However, we did not retain this definition as tests revealed that it does not satisfy a log-normal distribution and degraded the correlations with observations when used in (11).

Log-normal fits for the different turbulent indices

Table 2 summarizes the log-normal fits to the pdfs in Figure 1 as defined by (3).

Table 2: Fits for mean and variance of the log-normal distributions

Index	μ	σ^2
Ellrod1	-15.4	1.25
F3D	-16.3	1.80
MWT	-6.15	2.50
GWD	-2.20	0.52
DISS	-3.30	0.60

References

Beljaars, A. C. M., A. R. Brown, and N. Wood, 2004: A new parametrization of turbulent orographic form drag. *Q. J. R. Meteorol. Soc.*, **130**, 1327–1347.

Cornman, L. B., C. S. Morse, and G. Cunning, 1995: Real-time estimation of atmospheric turbulence severity from in-situ aircraft measurements. *J. Aircr.*, **32**, 171–177, doi:10.2514/3.46 697.

Ellrod, G. P. and D. I. Knapp, 1992: An objective clear-air turbulence forecasting technique: verification and operational use. *Wea. Forecasting*, **7**, 150–165, doi:/10.1175/1520–0434(1992)007<0150:AOCATF>2.0.CO;2.

Hoblit, F. M., 1988: *Gust loads on aircraft: concepts and applications*. IAA Education Series, Institute of Aeronautics and Astronautic, 306 pp. pp.

Holton, J. R., 2004: *An introduction to dynamic meteorology*. Academic Press, 4 ed. pp.

Kim, J.-H., R. Sharman, M. Strahan, J. Scheck, C. Bartholomew, J. C. H. Cheung, P.Buchanan, and N. Gait, 2018: Improvements in nonconvective aviation turbulence prediction for the world area forecast system. *Bull. Am. Meteorol. Soc.*, **99**, 2295–2311,doi:10.1175/BAMS–D–17–0117.1.

Lane, T. P., J. D. Doyle, R. Plougonven, M. A. Shapiro, and R. D. Sharman, 2004: Observations and numerical simulations of inertia-gravity waves and shearing instabilities in the vicinity of a jet stream. *J. Atmos. Sci.*, **61**, 2692–2706,doi:10.1175/JAS3305.1.

Louis, J.-F., 1979: A parametric model of vertical eddy fluxes in the atmosphere. *Bound. Layer Meteor.*, **17**, 187–202.

Orr, A., P. Bechtold, J. F. Scinocca, M. Ern, and M. Janiskova, 2010: Improved middle atnosphere climate and forecasts in the ECMWF model through a non-orographic gravity wave drag parametrization. *J. Climate*, **23**, 5905–5926.

Sharman, R., L. B. Cornman, G. Meymaris, J. Pearson, and T. Farrar, 2014: Description and derived climatologies of automated in situ eddy dissipation rate reports of atmospheric turbulence. *J. Appl. Meteor. Climatol.*, **53**, 1416–1432, doi:10.1175/JAMC–D–13–0329.1.

Sharman, R. D. and J. Pearson, 2017: Prediction of energy dissipation rates for aviation turbulence. Part I: Forecasting nonconvective turbulence. *J. Appl. Meteor. Climatol.*, **56**, 317–337, doi:10.1175/JAMC–D–16–0205.1.

Shutts, G., 2015: A stochastic convective backscatter scheme for use in ensemble prediction systems. *Q. J. R. Meteorol. Soc.*, **141**, 2602–2616, doi:10.1002/qj.2547.

Williams, P. D. and M. M. Joshi, 2013: Intensification of winter transatlantic aviation turbulence in response to climate change. *Nat. Clim. Change*, **3**, 644–648.